

Supplement of Atmos. Meas. Tech., 12, 3183–3208, 2019
<https://doi.org/10.5194/amt-12-3183-2019-supplement>
© Author(s) 2019. This work is distributed under
the Creative Commons Attribution 4.0 License.



Supplement of

A high-speed particle phase discriminator (PPD-HS) for the classification of airborne particles, as tested in a continuous flow diffusion chamber

Fabian Mahrt et al.

Correspondence to: Fabian Mahrt (fabian.mahrt@env.ethz.ch) and Zamin A. Kanji (zamin.kanji@env.ethz.ch)

The copyright of individual parts of the supplement might differ from the CC BY 4.0 License.

S1 Introduction

This supporting information provides additional text and figures to support the main manuscript.

S2 Symmetrical ice crystals

Figure S1 depicts the complete 2D scattering pattern of a hexagonal ice crystal as obtained from SID3. If oriented in such a way that the resulting scattering pattern on the linear CMOS arrays of PPD-HS appears symmetrical, ice crystals can become classified as spherical by our random forest model. This illustrates the shortcoming of using reduced scattering to assess particle shape and can partly explain the classification of some ice crystals as spherical (see main text Sect. 4.3).

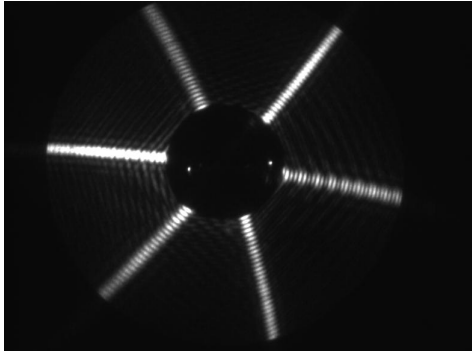


Figure S1. Example 2D scattering pattern captured by SID3 of a hexagonal ice crystal, illustrating the a six-fold symmetry of the diffraction pattern. Image from C. Stopford.

S3 Fibre particles

In Fig. S2 we show a random selection of scattering patterns obtained from the fly ash solution. While some particles (e.g. 10 1,3 and 8) show a distinct spike in scattering intensity along both arrays, other particles (e.g. 4, 13) show scattering patterns that cannot unambiguously be attributed to fibres, which is expected given smaller spherical or aspherical residuals could also result from the fly ash suspension.

In Fig. S3 we depict the relative probability of a CMOS array pixel to be associated with the maximum light scattering intensity of the captured pattern for fibrous particles, to support our argument in the main text about fibre alignment within a laminar flow. Here, a particle was required to have a minimum PTM value of 5 and minimum variance values of 100 along both arrays to be considered a fibre, sampling from the fly ash data set. The clustering of pixels around the (physical) center of 15 the CMOS arrays demonstrates the preferential alignment of fibres along the flow axis.

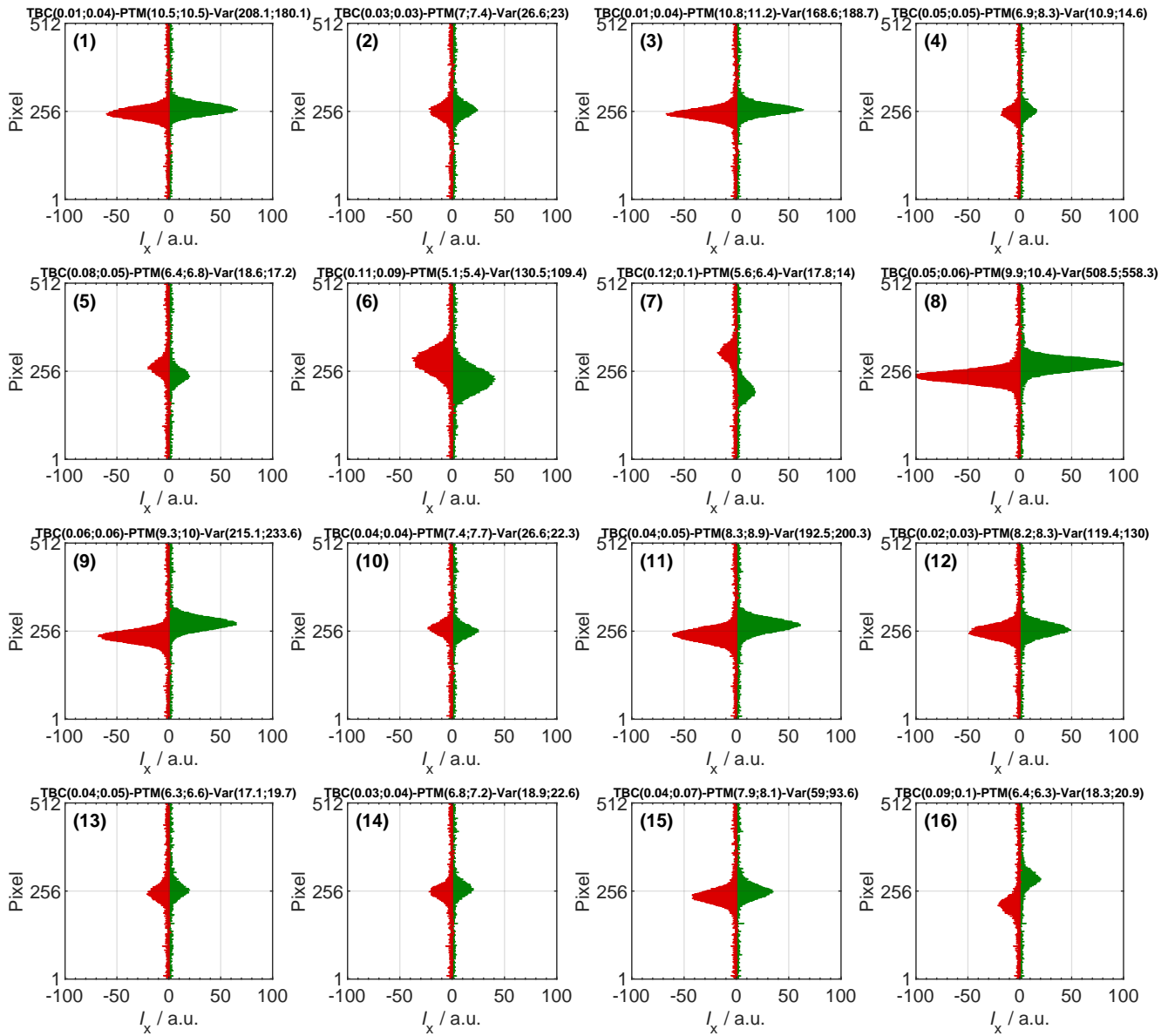


Figure S2. Example scattering patterns of particles from the coal fly ash suspension. Plots depict the relative light intensity as a function of array pixel number, for array 1 (green) and array 2 (red). The values on top of each panel depict the TBC and variance, where the first number corresponds to array 1 and the second number to array 2, respectively, as well as the PTM.

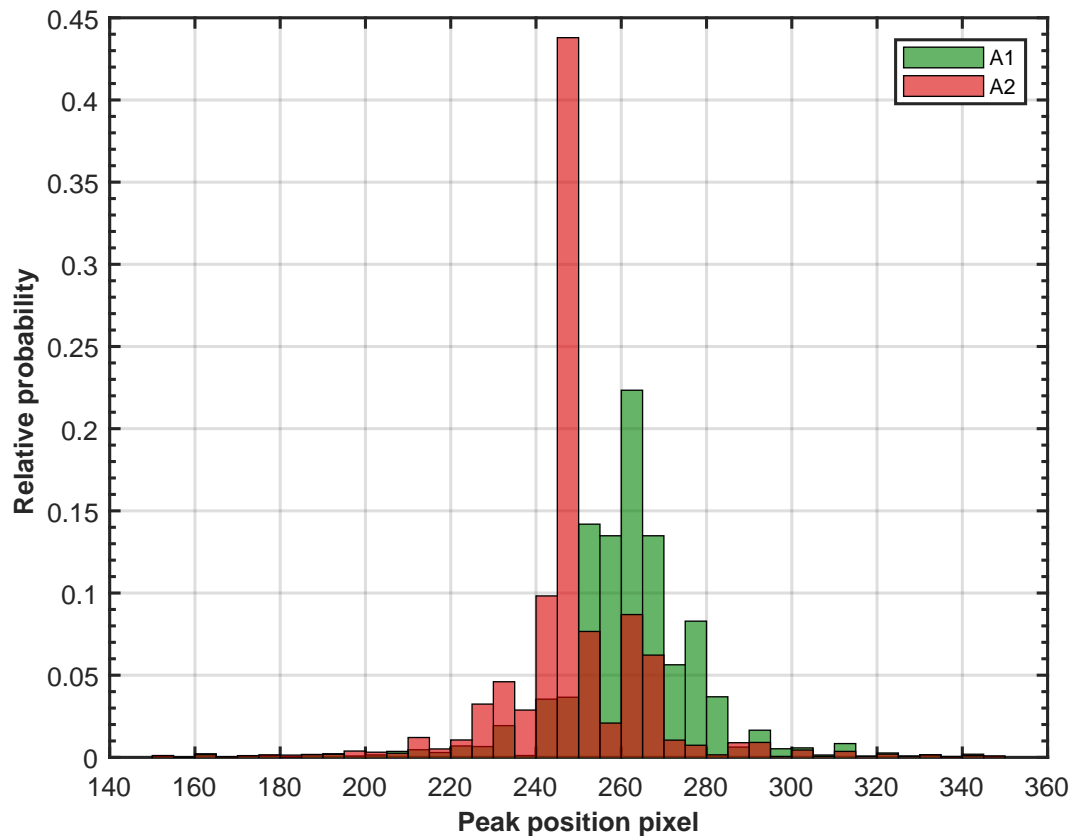


Figure S3. Histogram showing the relative probability of a CMOS array pixel to be associated with the maximum light scattering intensity for fibre particles. Fibre particles were identified as having minimum PTM value of 5 and minimum variance values of 100.

S4 Electronic configuration of PPD-HS

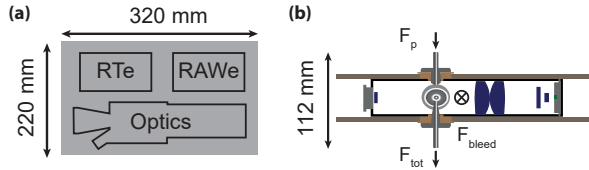


Figure S4. Schematic illustrating the dimensions of PPD-HS (a) from top along with the different electronic boards and (b) from the side showing the flow configuration as described in the main text. RTe and RAWe denote the real time and the raw electronics board, respectively.

There are two different sets of electronics reading out the CMOS data. Both boards are based around a Field Programmable Gate Array (FPGA), using a Spartan-III XC3S200AN (Xilinx, Frankfurt, Germany) and a Spartan-II XC2S50-PQ208, respectively. The raw-electronics are connected to a computer via a QuickUSB 2.0 board (BitWise Systems, Santa Barbara, USA), and the RT-electronics via a Serial Peripheral Interface (SPI) interface.

The readout of the RT-electronics is triggered by an analogue circuit detecting an intensity peak from the photo diode. It stores this peak value for later conversion to particle size, and controls the pulsing of the image laser, as described in the main text. When the RT-electronics begins readout of the CMOS arrays, it signals the raw-electronics to readout simultaneously. Thus, the raw-electronics are not connected to the photo diode and thus its output does not contain any information on particle size. If either board is still processing when another particle arrives, that board will not readout that trigger. This means that particle information of the two electronic boards are complementary but not congruent, with the raw sampling a subset of the particles detected by the RT. Thus information of both FPGAs cannot be compared on a PbP basis. Both boards are controlled via a software package written in C#. A graphical user interface displays time series of the shape indicators available from the RT-electronics, along with a particle size histogram. From the raw-electronics a series of individual scattering patterns are displayed as they are captured.

S4.1 raw-electronics: Absence of optical particle size information

The raw data does not contain information on the optical particle size, as it is not directly connected to the photo diode. Estimation of particle size from the resulting scattering pattern would require normalization to the integration duration of the detector arrays, but seems not feasible, as shown in Fig. S5. Here we show box plots of the integrated scattering intensities of both CMOS arrays for exemplary data sets of spherical PEG particles of different size. While there is good agreement between the two arrays at a given size along with a general increase in integrated scattering intensities for increasing particle size, determination of particle sizes is ambiguous due to the significant overlap of the box plots corresponding to different particle sizes. This is consistent with the variation in scattering intensities discussed for Fig. A2 in the main text.

In Fig. S6 we depict raw scattering pattern of $2\text{ }\mu\text{m}$ PSL particles, considered the lower size limit at which particles can be detected by PPD-HS.

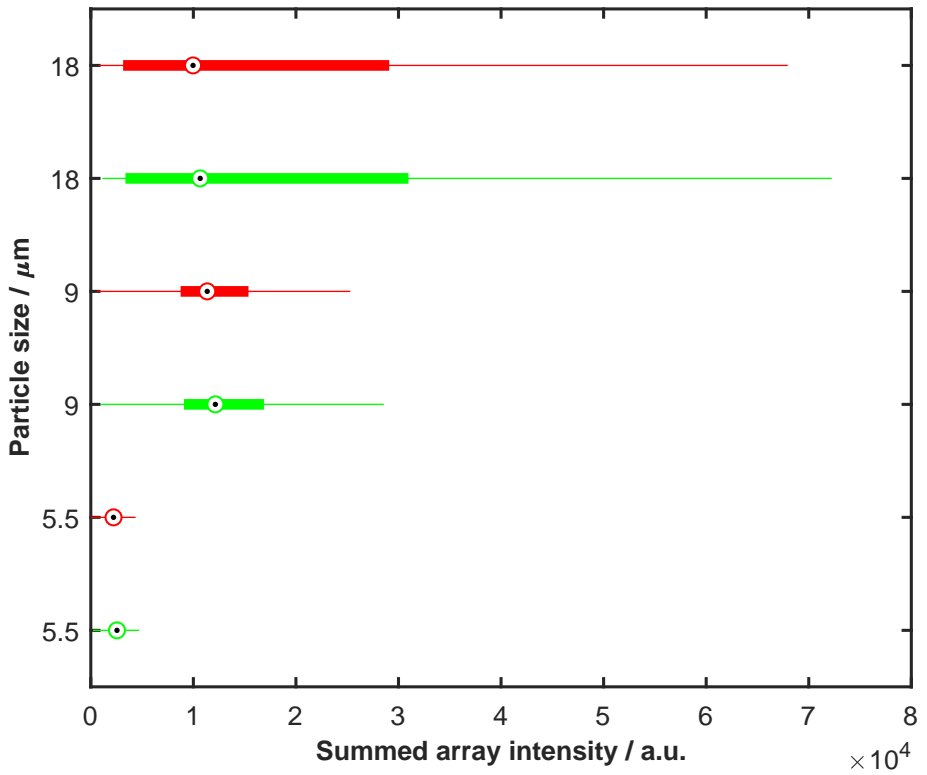


Figure S5. Box plots showing the summed scattered light intensity captured by CMOS array 1 (green) and array 2 (red) for exemplary spherical PEG particles of different sizes. For each box, the black dot indicates the median, and the bottom and top edges correspond to the 25th and 75th percentiles, respectively. Whiskers extend to the most extreme data points not considered outliers, which are not shown for clarity.

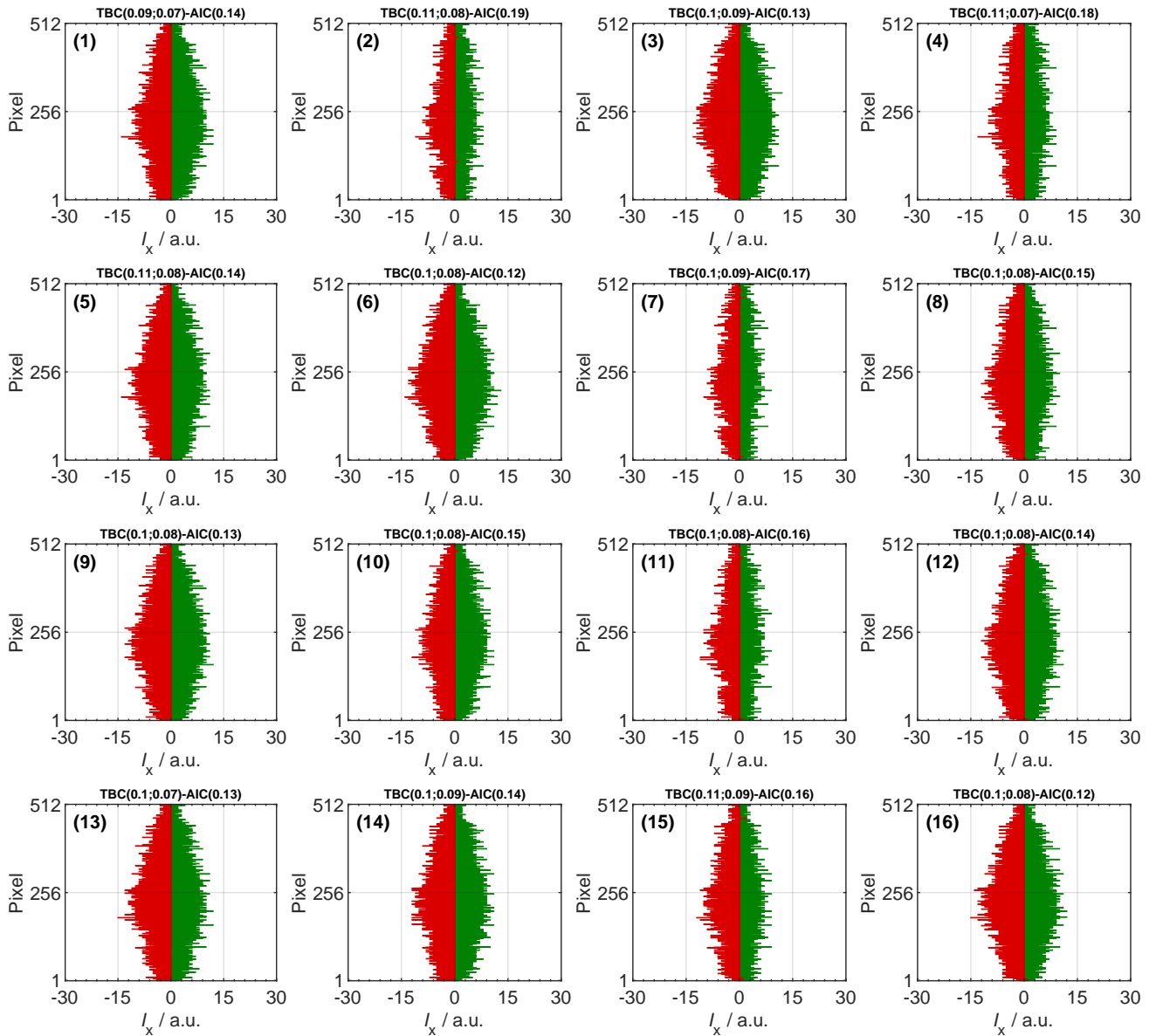


Figure S6. Example scattering patterns from 2 μm PSL particles. Plots depict the relative light intensity as a function of array pixel number, for array 1 (green) and array 2 (red). The values on top of each panel depict the TBC values, where the first number corresponds to array 1 and the second number to array 2, respectively, as well as AIC value.

S5 CMOS detector arrays

S5.1 Background intensities

Scattering data recorded by PPD-HS is background corrected. Therefore, prior to each experiment the image laser is (artificially) triggered by the operator, when no flow and thus no particle are present within the optics block of PPD-HS. The light

5 intensities recorded by the individual pixels of the CMOS arrays are stored and subtracted accordingly from the scattering patterns recorded for each particle imaged by PPD-HS. In Fig. S7a and b we exemplary show the background intensities recorded by both arrays. Note the difference in intensity (scale) compared to e.g. the examples shown in main text Fig. 2.

From the difference in background intensities recorded by the two arrays it becomes apparent that an separate background correction for each array/pixel is essential. In order to evaluate the variation in the background, we recorded multiple back-

10 ground files over the course of an experiment and compared to the initial background intensities. In Fig. S7c and d we display the difference in intensities for CMOS array 1 and 2, respectively, between the initial background taken at 10:30 am and the background recorded at a later time, as indicated. Over the period of roughly 2 h between the initial background (10:30 am)

15 and the last background (11:52 am) CMOS array1 shows both a smaller reduction in background intensities (absolute values) and less variation over time, compared to array 2. The reduction in background intensities likely results from a warm up of the

15 CMOS arrays over time, as the image laser laser is pulsed and the near-forward scattering of particles is recorded. Given the similarity in background intensities after roughly 15 min (10:46) and 2 h (11:52) (see Fig. S7c and d), we suggest to operate

PPD-HS for about 15 min and then take a new background prior to starting the experiment in oder to avoid overcorrection of the detector signal form imaged particles, also the time ultimately depends on the number of times the image laser is pulsed.

In case the scattering of a particle is small and/or the background intensity is high the resulting scattering pattern can reveal

20 negative intensity values, as exemplified in Fig. S8. In order to limit this over correction, the background is automatically recorded by PPD-HS' electronics at user defined intervals. Nevertheless, it is worth wile noting that variance values of par-

ticles associated with negative intensities can be rather large (e.g. particles 1 and 2 in Fig. S8). Consequently, such particles do not get recognized as noise by the variance criterion (see Appendix B). In fact, the scattering patterns depicted in Fig. S8

25 stem from a data set of spherical PEG particles. The TBC values associated with these particles are high, as can be seen by the values indicated on top of the scattering patterns. In order to remove such particles prior to using this data within our decision

tree model, criteria other than a minimum variance value need to be applied, to recognize noise particles in data sets, which are

54 affected by a large background intensities.

S5.2 Electronic noise

In addition to the background intensities on the CMOS arrays caused by flashing the image laser in the absence of particles in

30 the scattering chamber, the pixels perceive intensities due to electronic noise. Electronic noise corresponds to intensity values recorded by the CMOS arrays at a given background intensity. In order to simulate this effect, we recorded 6000 background

35 files (*blind particles*) when the inlet was closed, such that no particles can enter. For each of these blind particles the mean of all backgrounds was subsequently subtracted from the scattering pattern, to avoid a bias from a dynamically changing background,

resulting in the remaining intensity values, which we refer to as electronic noise. In Fig. S9 we show examples of this electronic

noise. From there, it is evident that the intensity signal of the electronic noise is around $I = \pm 3$ a.u. on each array.

S5.3 Electronic dead time and sample volume reduction

The frame rate determining factor for particle detection is the dead time of the CMOS arrays, given as:

$$\tau(\mu s) = 177 + \frac{Int_{delay}}{48} + \frac{Int_{duration}}{3}, \quad (S1)$$

where Int_{delay} denotes the delay time between particle detection by the photo diode and start of the image recording by the

40 CMOS arrays and $Int_{duration}$ denotes the duration for which the image laser is switched on (pulse duration; see Fig. 1c in main text). The factors 48 and 3 in Eq. (S1) are conversion factors needed to convert the time of the electronic boards from ticks

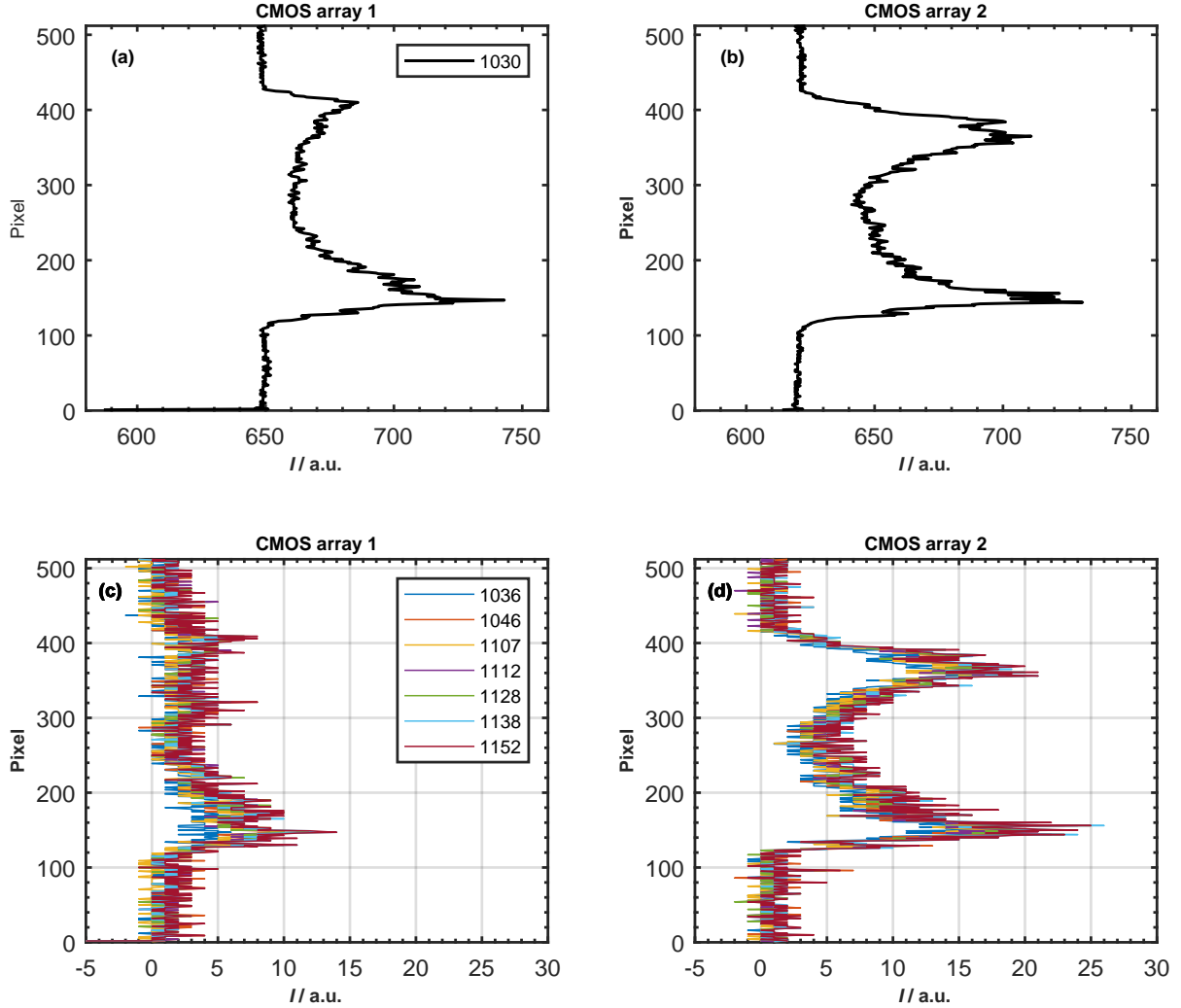


Figure S7. Example of the background light intensities captured by (a) CMOS array 1 and (b) CMOS array 2. (c) and (d) show the change in CMOS background over time, given as difference between the initially captured background intensities (panels a and b, respectively) and the background recorded at the time indicated. Time stamps in the legend are shown in terms of HHMM.

(system clock) to an absolute time in microseconds. This results in an electronic dead time of PPD-HS ranging from $177\text{ }\mu\text{s}$ to $267\text{ }\mu\text{s}$ based on the flow rate through the system.

In Fig. S10 we plot the CMOS array dead time, τ_{CMOS} , denoting the time needed to process the captured light intensities during which no scattering pattern of other particles can be recorded. Values for τ_{CMOS} are calculated using Eq. S1.

Particles passing the PPD-HS sensing volume during this dead time are not recorded, leading to a reduced effective sample volume as shown by Johnson et al. (2014). Figure S11 shows the percentage missed particles as a function of CMOS dead time and particle number concentration for $F_{\text{tot}} = 2.83 \text{ Lmin}^{-1}$, corresponding to the total flow rate in HINC. Taking, for instance, particle number concentration of 20 cm^{-3} and a dead time of $262 \text{ }\mu\text{s}$ (for typical operation conditions of $Int_{\text{delay}} = 5 \text{ }\mu\text{s}$ and $Int_{\text{duration}} = 255 \text{ }\mu\text{s}$) results in a reduction of total particles detected by PPD-HS of 24.7 %. In other words, given a volume of

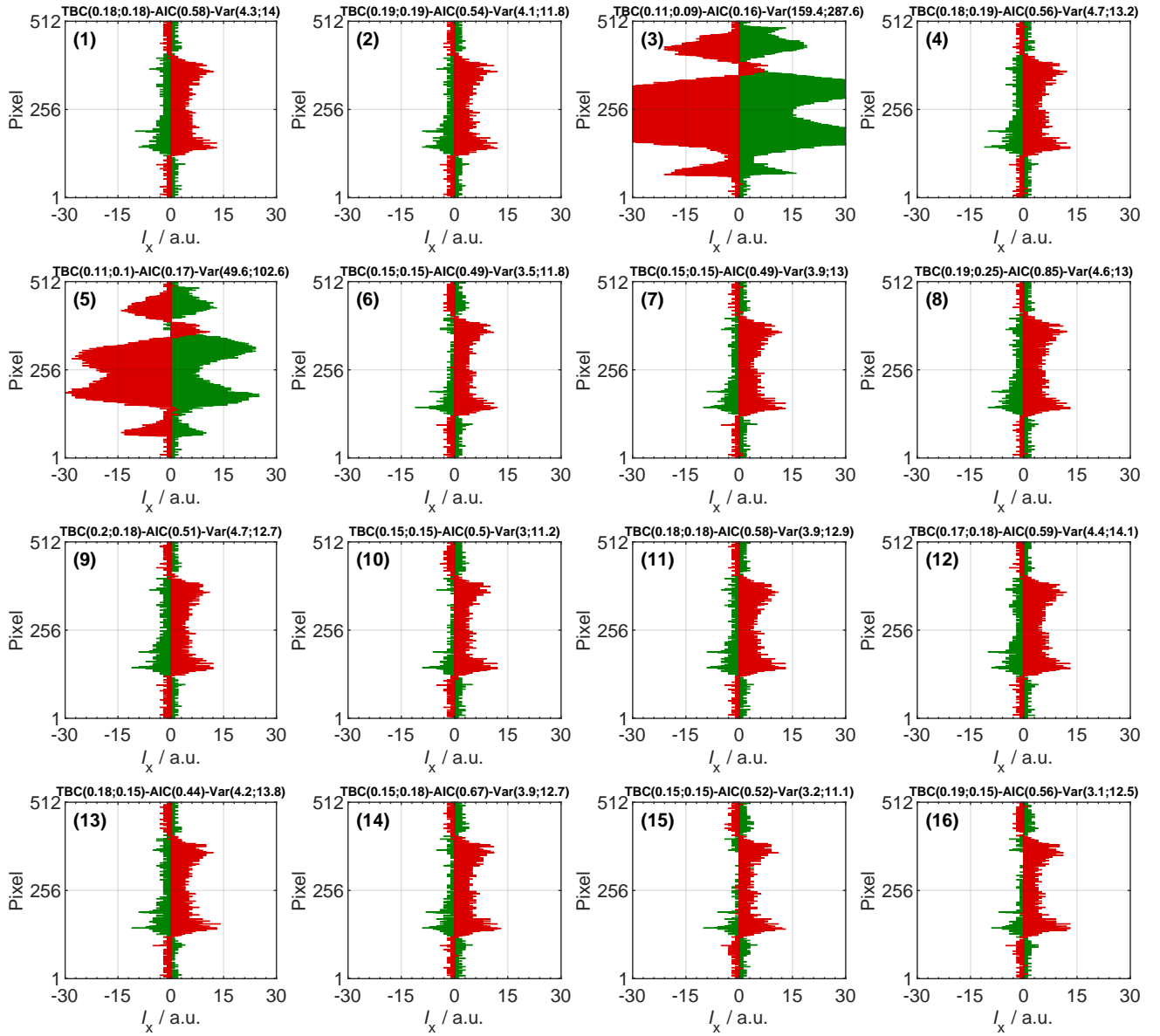


Figure S8. Example scattering patterns as obtained from the raw-FPGA, where high background intensities cause negative intensity values for background corrected data shown. Plots depict the relative light intensity as a function of array pixel number, for array 1 (green) and array 2 (red). The values on top of each panel depict the TBC, mean scattering intensity and variance, where the first number corresponds to array 1 and the second number to array 2, respectively.

2.83 L (sampled with HINC) only 2.13 L are effectively sampled by PPD-HS, thus the number of detected particles needs to be normalized to this volume, to derive representative particle number concentrations. Overall the percentage of missed particles increases stronger with increasing ambient particle number concentration, as compared to increasing CMOS dead time, as can

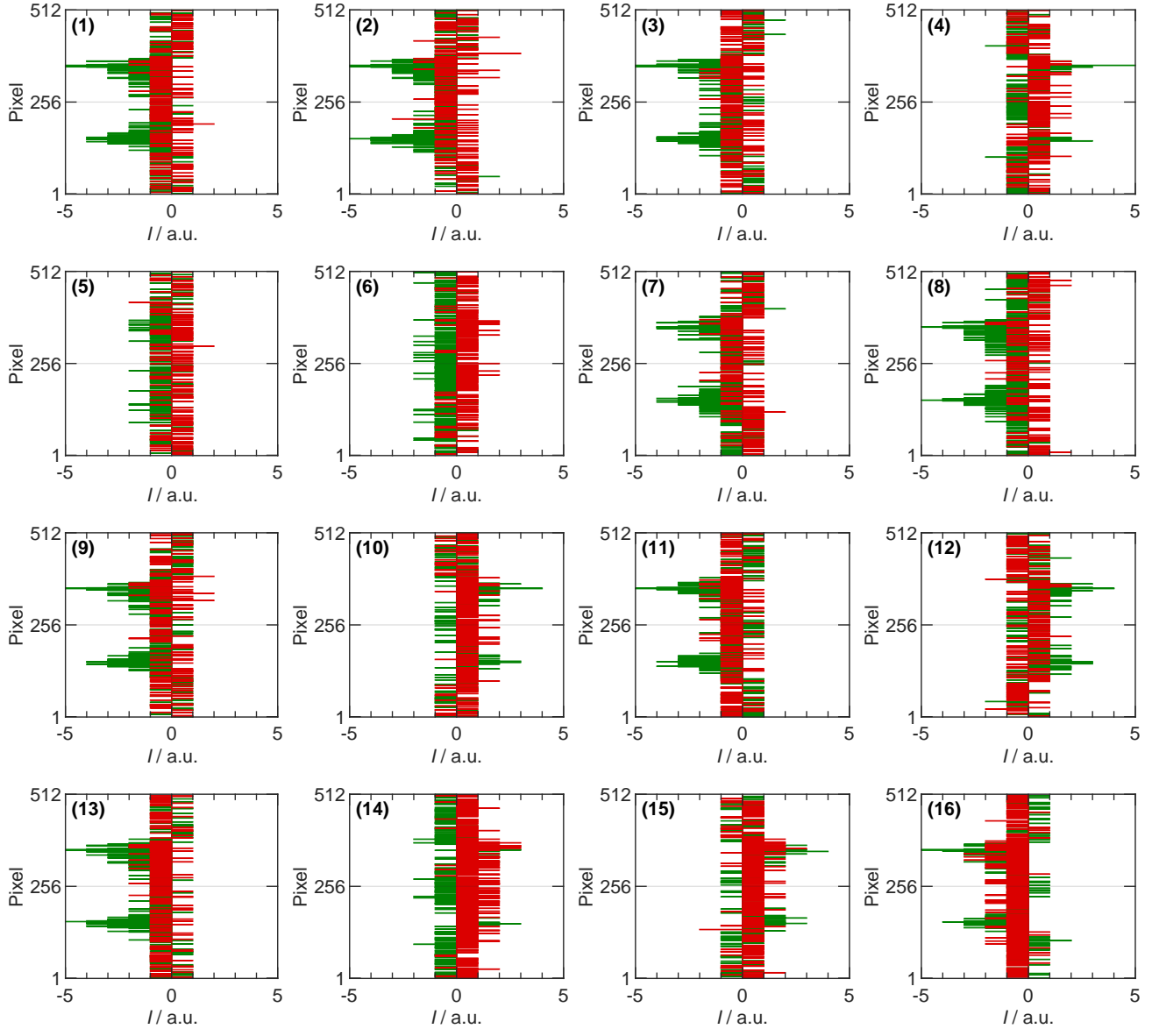


Figure S9. Example scattering patterns showing the electronic noise of the CMOS arrays, i.e. captured when no flow (particle) was present within the optics block.

easily be seen from Fig. S11 when comparing the change in missed particles along isolines of dead time and isolines of particle concentration, respectively.

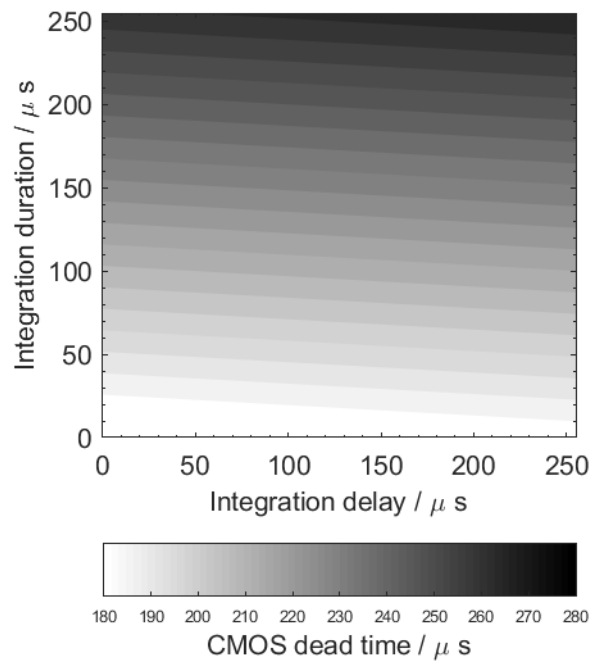


Figure S10. Electronic dead time of the CMOS arrays in PPD-HS as a function of integration delay and integration duration calculated using Eq. S1.

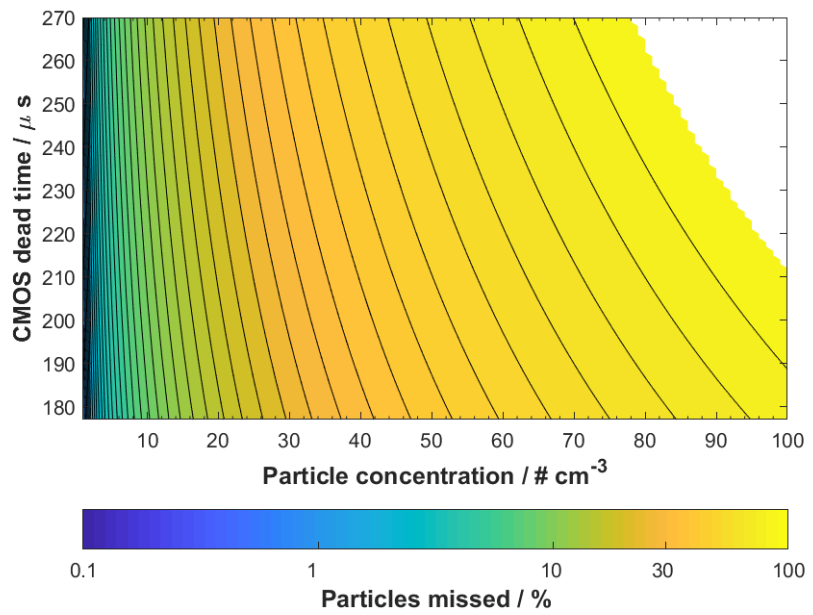


Figure S11. Missed particles in percentage, calculated using Eq. S1, as a function of CMOS array dead time (see Fig. S10) and particle number concentration. Calculations were done for a sample flow rate of 2.83 Lmin^{-1} used in PPD-HS HINC measurements. White areas indicate where the reduction exceeds 100 %.

S6 Calibration data sets

Table S1: Overview of calibration data sets of PPD-HS along with information on the particle size distribution characteristics from RT electronics and from APS measurements operated in parallel. Data set ID denotes the name of the data set, N_{tot} the number of particles contained, max. FR the maximal frame rate observed in units of [$\#\text{s}^{-1}$] and aerosol indicates the particle type. For the APS measurements we report \bar{d}_a the mean aerodynamic size, σ_a the standard deviation of the aerodynamic mean diameter, $d_{a,g}$ the aerodynamic geometric mean diameter and $\sigma_{a,g}$ the geometric mean standard deviation. NaN values indicate sizes out of the range of the APS. From the RT-electronics we report \bar{d}_o the mean optical size, σ_o the standard deviation of the optical mean diameter, $d_{o,g}$ the optical geometric mean diameter and $\sigma_{o,g}$ the geometric mean standard deviation. All sizes are given in unit of [μm]. The datasets highlighted in bold are those used in Fig. S12.

Data set ID	N_{tot}	max. FR	Aerosol	\bar{d}_a	σ_a	$d_{a,g}$	$\sigma_{a,g}$	\bar{d}_o	σ_o	$d_{o,g}$	$\sigma_{o,g}$
20170720-162928	6213	27	PSL	1.58	0.30	1.44	1.82	2.18	2.56	1.99	1.32
20170721-143734	8663	27	PSL	1.69	1.43	1.26	2.48	2.94	0.75	2.88	1.22
20170721-145907	8257	26	PSL	1.76	1.43	1.32	2.50	2.91	0.51	2.86	1.21
20170725-153555	14490	30	PSL	1.89	1.48	1.43	2.55	2.89	0.71	2.84	1.22
20170725-160926	15571	29	PSL	1.91	1.44	1.46	2.56	2.90	0.55	2.85	1.20
20170726-160127	25910	45	PSL	0.98	0.99	0.77	1.84	4.00	1.18	3.84	1.35
20170726-162402	27279	57	PSL	1.02	1.10	0.79	1.89	3.94	1.09	3.78	1.36
20170825-171127	105696	57	PEG	6.39	0.56	6.27	1.30	6.33	2.20	5.92	1.47
20170825-171435	175096	57	PEG	6.39	0.56	6.27	1.29	6.28	1.99	5.89	1.47
20170825-172154	68909	57	PEG	6.42	0.25	6.38	1.16	6.32	1.99	5.94	1.46
20170825-172423	272295	57	PEG	6.40	0.22	6.37	1.13	6.29	1.94	5.92	1.46
20170825-154025	184216	57	PEG	7.21	0.59	7.13	1.21	7.05	2.37	6.58	1.48
20170825-155323	170932	57	PEG	7.18	0.81	7.04	1.30	7.09	2.45	6.57	1.52
20170825-160551	160483	57	PEG	7.97	0.43	7.89	1.22	8.42	2.49	7.95	1.44
20170825-161520	169903	57	PEG	7.99	0.18	7.97	1.10	8.52	2.66	7.98	1.48
20170825-163250	80076	57	PEG	9.05	0.43	8.99	1.18	9.86	2.93	9.31	1.44
20170825-164354	116718	57	PEG	8.56	4.20	7.72	1.95	9.58	2.98	8.96	1.49
20170828-110707	107496	57	PEG	8.03	0.45	7.96	1.21	8.94	2.61	8.43	1.45
20170828-111200	465243	57	PEG	7.18	0.21	7.15	1.11	6.62	2.46	6.08	1.55
20170828-102955	87763	57	PEG	7.92	1.78	7.55	1.54	8.94	2.61	8.43	1.45
20170828-103643	305151	57	PEG	7.87	1.68	7.51	1.53	9.30	2.24	8.92	1.38
20170828-104639	48410	919	PEG	7.81	2.48	7.29	1.68	9.09	2.45	8.67	1.40
20170828-104853	280162	919	PEG	8.03	0.44	7.96	1.21	9.01	2.33	8.60	1.40
20170828-115259	294999	919	PEG	7.00	15.91	4.50	3.80	11.01	2.35	10.65	1.34
20170828-120202	159738	919	PEG	9.26	0.90	9.16	1.28	8.72	3.44	7.97	1.56
20170828-112856	294910	919	PEG	7.77	8.18	6.23	2.51	9.06	2.85	8.50	1.46
20170831-183318	52378	919	PEG	3.10	0.03	3.09	1.21	3.30	0.64	3.22	1.25
20170831-183701	53921	919	PEG	3.09	0.03	3.09	1.21	3.31	0.69	3.24	1.24
20170831-174520	42437	1014	PEG	3.84	0.03	3.84	1.13	3.74	0.85	3.62	1.30
20170831-173416	51468	1014	PEG	4.38	0.03	4.37	1.17	3.92	1.10	3.75	1.36
20170831-173843	70399	1014	PEG	4.34	0.04	4.34	1.12	3.93	1.10	3.77	1.36
20170831-163954	77431	1014	PEG	4.74	0.07	4.74	1.24	4.52	1.35	4.27	1.43
20170831-164356	75422	1014	PEG	4.75	0.07	4.74	1.22	4.53	1.34	4.29	1.42
20170831-161103	1290	1014	PEG	5.45	0.04	5.44	1.29	5.15	1.68	4.80	1.50
20170831-162528	26885	308	PEG	6.34	0.08	6.33	1.06	6.04	2.02	5.60	1.52
20170831-163046	25493	302	PEG	6.32	0.07	6.31	1.06	6.04	2.04	5.61	1.52

20171004-130401	84050	302	PEG	8.47	0.25	8.45	1.23	8.70	2.78	8.12	1.51
20171004-131401	78355	302	PEG	8.50	0.29	8.47	1.22	8.76	2.88	8.11	1.55
20171004-132402	79450	302	PEG	8.77	0.30	8.75	1.14	8.78	2.95	8.09	1.57
20171004-133401	87192	302	PEG	8.81	0.34	8.78	1.16	8.62	2.98	7.91	1.58
20171009-113943	85969	302	PEG	5.09	0.08	5.07	1.31	4.94	1.52	4.64	1.46
20171009-114308	80686	302	PEG	5.07	0.07	5.06	1.40	5.01	1.59	4.69	1.49
20171009-115227	71133	302	PEG	5.06	0.06	5.05	1.41	4.78	1.61	4.45	1.50
20171009-115501	91069	302	PEG	5.05	0.06	5.04	1.34	4.91	1.41	4.65	1.43
20171009-115926	89070	302	PEG	5.01	0.15	4.99	1.19	4.78	1.54	4.47	1.48
20171009-120232	26577	321	PEG	4.99	2.83	4.50	1.72	5.50	2.03	5.05	1.55
20171101-100451	147199	321	PEG	3.84	2.64	3.38	1.74	4.93	1.66	4.59	1.50
20171101-101921	135939	321	PEG	4.99	0.25	4.92	1.24	4.88	1.55	4.58	1.46
20171101-104024	119169	321	PEG	4.94	0.51	4.80	1.37	4.59	1.56	4.28	1.48
20171101-105216	119731	321	PEG	5.00	0.24	4.94	1.23	4.65	1.59	4.33	1.48
20171101-110539	119306	321	PEG	4.91	0.70	4.71	1.46	4.80	1.67	4.47	1.49
20171101-111701	95865	321	PEG	4.98	0.36	4.88	1.30	4.89	1.61	4.56	1.49
20171101-112820	108205	321	PEG	4.99	0.33	4.90	1.28	5.06	1.64	4.72	1.49
20171101-114001	87727	321	PEG	5.03	0.22	4.98	1.22	4.72	1.82	4.29	1.60
20171101-115138	114612	321	PEG	4.97	0.41	4.86	1.33	5.05	1.62	4.72	1.49
20171113-160743	27858	795	PEG	4.17	0.67	3.97	1.50	3.94	1.07	3.77	1.38
20171113-161101	20567	918	PEG	4.08	0.03	4.07	1.38	3.62	1.38	3.45	1.38
20171115-151722	135697	918	PEG	6.26	0.11	6.24	1.11	6.09	2.04	5.66	1.51
20171115-152533	191482	918	PEG	5.93	0.10	5.92	1.15	6.00	2.00	5.58	1.52
20171116-100536	94752	918	PEG	5.58	0.25	5.56	1.21	5.37	1.89	4.97	1.52
20171116-103905	84793	918	PEG	5.55	0.42	5.51	1.17	5.82	1.96	5.43	1.49
20171116-105058	110046	918	PEG	5.55	0.42	5.55	1.18	5.78	1.95	5.39	1.49
20171117-112601	87184	918	PEG	8.86	0.15	8.85	1.13	10.02	2.90	9.45	1.46
20171120-153103	13227	131	PEG	1.67	0.01	1.67	1.07	1.88	0.70	1.85	1.18
20171120-155231	78650	131	PEG	3.39	0.02	3.39	1.05	3.33	0.90	3.22	1.31
20171120-163954	87602	131	PEG	5.34	0.53	5.30	1.18	5.13	1.88	4.74	1.53
20171120-120502	100679	131	PEG	9.22	0.59	9.18	1.11	10.01	3.15	9.41	1.46
20171121-104421	114866	131	PEG	8.54	1.12	8.47	1.21	9.38	3.27	8.65	1.54
20180112-135742	121418	131	PEG	3.32	0.25	2.97	1.91	3.71	0.89	3.58	1.32
20180112-140601	122161	131	PEG	3.44	0.04	3.43	1.09	3.71	0.90	3.58	1.32
20180112-142536	63029	131	PEG	5.39	0.26	5.32	1.98	5.39	1.37	5.16	1.38
20180112-143527	61891	131	PEG	5.52	0.17	5.48	1.17	5.59	1.52	5.32	1.41
20180112-141819	43571	932	PEG	4.99	0.10	4.97	1.24	4.45	1.32	4.22	1.41
20180112-142033	191015	932	PEG	5.26	0.34	5.19	1.41	5.33	1.47	5.08	1.40
20180706-152135	21787	240	PEG	15.63	3.85	15.43	1.22	11.09	7.10	9.20	1.84
20180809-140618	166104	240	PEG	13.98	17.76	11.71	2.39	17.95	5.99	16.55	1.60
20180809-142119	90492	240	PEG	15.13	1.50	15.00	1.20	15.60	6.61	13.25	2.00
20180815-123915	57957	240	PEG	14.71	1.65	14.52	1.26	16.90	5.59	14.88	1.90
20180815-122633	68174	240	PEG	11.98	1.36	11.88	1.18	13.54	4.12	12.27	1.74
20180815-125801	8272	182	PEG	17.89	6.94	17.04	1.61	18.46	7.16	15.82	1.99
20180815-092800	91608	182	PEG	3.52	0.08	3.50	1.11	3.46	0.79	3.36	1.29
20180815-093558	58698	182	PEG	3.97	0.10	3.95	1.14	3.46	0.79	3.36	1.29
20180815-095212	58883	182	PEG	5.96	0.23	5.93	1.32	5.40	1.82	5.05	1.47
20180815-101851	85166	182	PEG	5.09	0.15	5.07	1.25	5.56	1.28	5.39	1.29
20180815-120206	114885	182	PEG	8.26	0.49	8.23	1.17	8.71	2.42	8.24	1.45

20180815-120913	82080	182	PEG	9.74	0.46	9.70	1.13	10.61	3.01	9.87	1.57
20180824-150724	38471	457	PEG	NaN	NaN	NaN	NaN	24.67	7.33	23.07	1.54
20170904-173049	38795	451	NaCl	8.33	0.34	8.31	1.17	6.99	2.19	6.64	1.41
20170927-120901	122354	451	NaCl	4.33	0.17	4.31	1.12	3.69	1.06	3.54	1.35
20170927-141010	194981	451	NaCl	4.55	0.22	4.53	1.18	3.87	1.2	3.69	1.38
20170927-141613	251701	451	NaCl	4.49	0.11	4.48	1.11	3.88	1.13	3.71	1.36
20170927-165041	34360	1086	NaCl	6.7	5.04	5.86	2.45	5.67	2.29	5.13	1.6
20170928-115709	69867	1086	NaCl	13.07	22.94	10.13	3.54	11.97	4.48	10.44	1.88
20170928-120227	74563	1086	NaCl	14.48	4.99	14.02	1.56	11.45	4.52	9.88	1.92
20170928-122132	145525	1086	NaCl	5.81	2.26	5.49	1.74	5.16	1.91	4.79	1.49
20170928-122512	137416	1086	NaCl	6.28	0.35	6.26	1.16	5	1.63	4.72	1.42
20170928-105955	136649	1086	NaCl	6.95	0.33	6.92	1.14	5.52	1.79	5.2	1.43
20170928-110915	77354	1086	NaCl	7.47	0.99	7.39	1.28	6.1	2.03	5.77	1.42
20170928-113816	134235	1086	NaCl	9.67	0.64	9.62	1.2	8.24	2.53	7.72	1.49
20170928-114414	127973	1086	NaCl	9.45	0.54	9.41	1.15	7.78	2.38	7.34	1.45
20180823-115744	100836	1086	NaCl	9.99	4.03	9.43	1.96	9.78	2.3	9.33	1.44
20180823-121830	84533	1086	NaCl	12.41	8.43	11.43	2.16	12.33	3.17	11.58	1.54
20180823-123515	52077	1086	NaCl	14.99	10.31	13.66	2.28	14.69	3.76	13.67	1.61
20180823-123829	78031	1086	NaCl	14.63	10.23	13.28	2.45	14.42	3.62	13.41	1.62
20180823-131442	22140	427	NaCl	15.4	36.51	11.15	4.2	16.42	5.75	14.5	1.86
20180823-131908	50818	427	NaCl	10.71	46.74	7.58	3.18	13.41	6.5	10.63	2.25
20180823-132148	76554	427	NaCl	15.59	25.49	12.42	3.67	16.47	4.42	15.06	1.73
20180823-144659	20546	160	NaCl	NaN	NaN	NaN	NaN	11.93	11.58	7.82	2.54
20180823-151237	27125	159	NaCl	NaN	NaN	NaN	NaN	21.34	16.63	12.56	3.34
20180823-153024	13641	138	NaCl	NaN	NaN	NaN	NaN	30.22	11.7	26.18	1.98
20180823-154514	38280	389	NaCl	NaN	NaN	NaN	NaN	23.29	9.33	20.12	1.98

S6.1 Distributions of shape indicators of calibration data set

In Fig. S13 we show the probability distributions of the shape predictor variables derived from our PCA and used within our random forest model, for all data particles constituting the calibration data set (see Tab. S1). The overlap of the curves for spherical and aspherical particles is further revealed in the scattering plot of the individual shape indicators shown in Fig. S14 and partly explains the misclassification discussed in the main text.

In Fig. S15 we show scattering patterns of spherical PEG particles. All particles shown fulfill all our selection criteria of minimum variance, PTM and average intensity. The patterns appear visually symmetric on and across both arrays, even though the TBC values indicated on top of each reveal that at least one of the arrays is associated with a relatively large value comparable to those observed for aspherical particles. Spherical particles with high TBC values likely result from (large) particles with relatively large light intensities recorded by the individual CMOS pixels. In case the scattering pattern is not exactly projected around the midpoints of both arrays, high TBC values easily result even for these symmetrical patterns. Similarly, some of the NaCl particles produced by the VOAG reveal symmetrical scattering patterns, which are consequently associated with relatively low TBC values (see Fig. S16). While most of these near-spherical NaCl particles show a symmetric scattering pattern along only one of the CMOS arrays, we cannot exclude NaCl particles from our calibration data set that show symmetry comparable to spherical PEG particles, without manual inspection of these particles. Thus, even though the TBC in general is a good measure for particle sphericity, an absolute threshold value above which all particles are considered aspherical cannot be applied. Overall, this is a shortcoming of using the particle measures within the random forest model, rather than the individual pixel information, as well as defining all VOAG produced PEG and NaCl particles as spherical and aspherical, respectively, at the absence of a manual check of the individual scattering patterns.

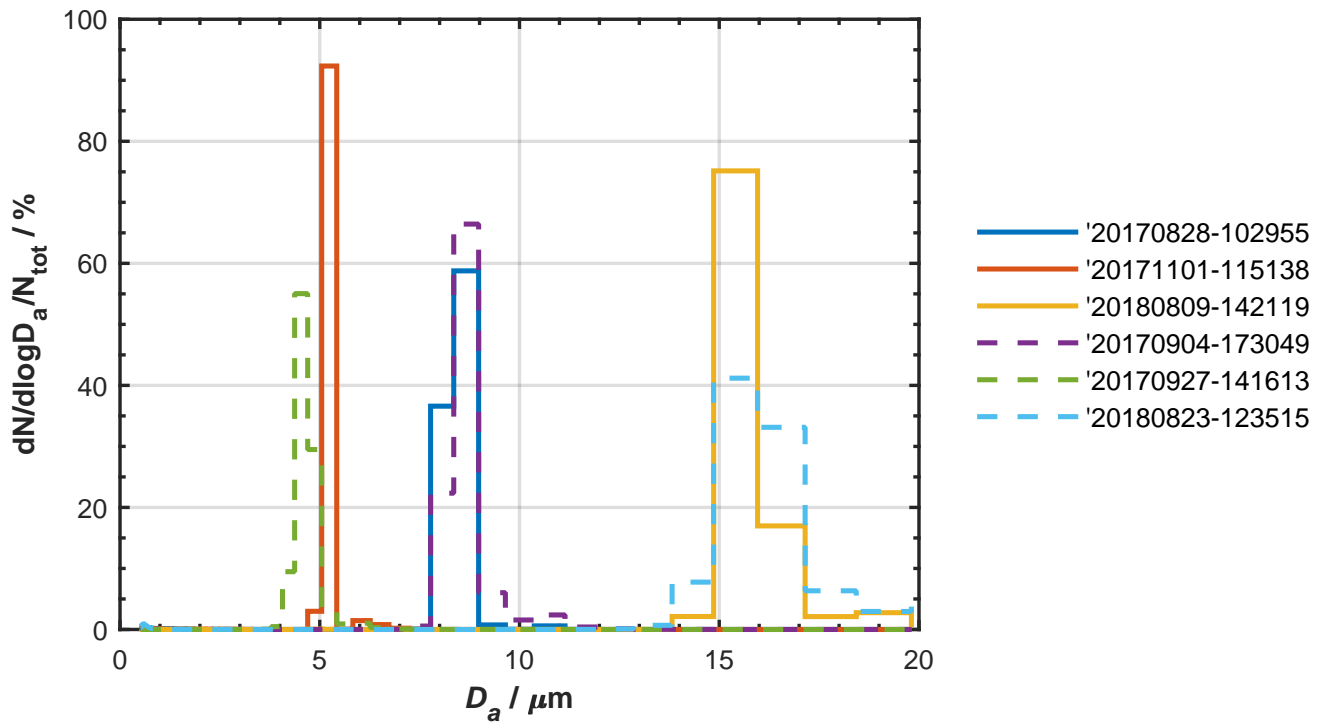


Figure S12. Example size distribution for selected calibration data sets, derived from APS measurements operated in parallel to PPD-HS. Curves denote mean distributions over period PPD-HS was operated and are given as percent lognormal distributions. Solid and dashed lines denote spherical and aspherical data sets, respectively, of comparable particle sizes. See Tab. S1 for details.

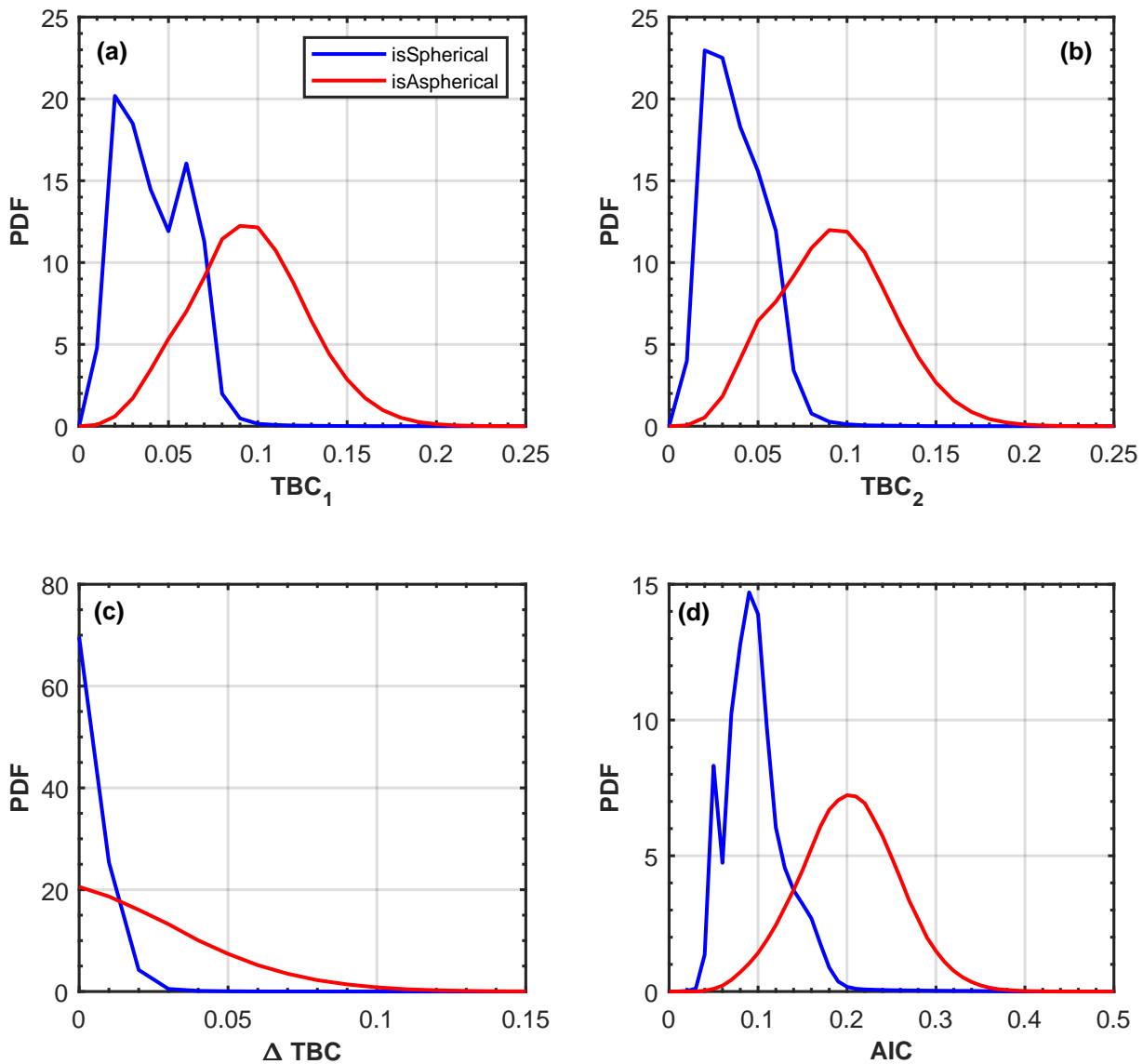


Figure S13. Probability density distribution of shape predictors for spherical (PEG) and aspherical (NaCl) particles, derived from calibration data set (see Tab. S1), showing (a) TBC_1 , (b) TBC_2 , (c) ΔTBC and (d) AIC.

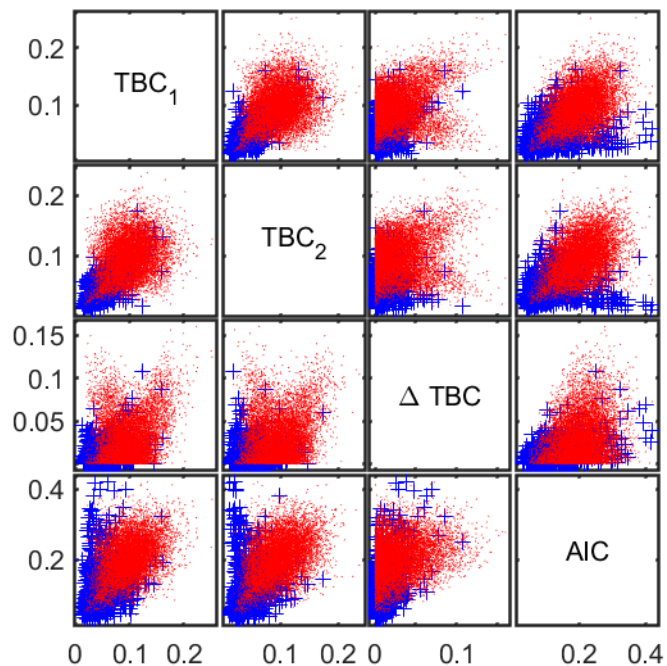


Figure S14. Scattering matrix relating the shape predictors for spherical (blue) and aspherical (red) particles, for a random subset of 5000 particles, encompassing an equal number of spherical and aspherical particles, respectively, derived from calibration data set (see Tab. S1).

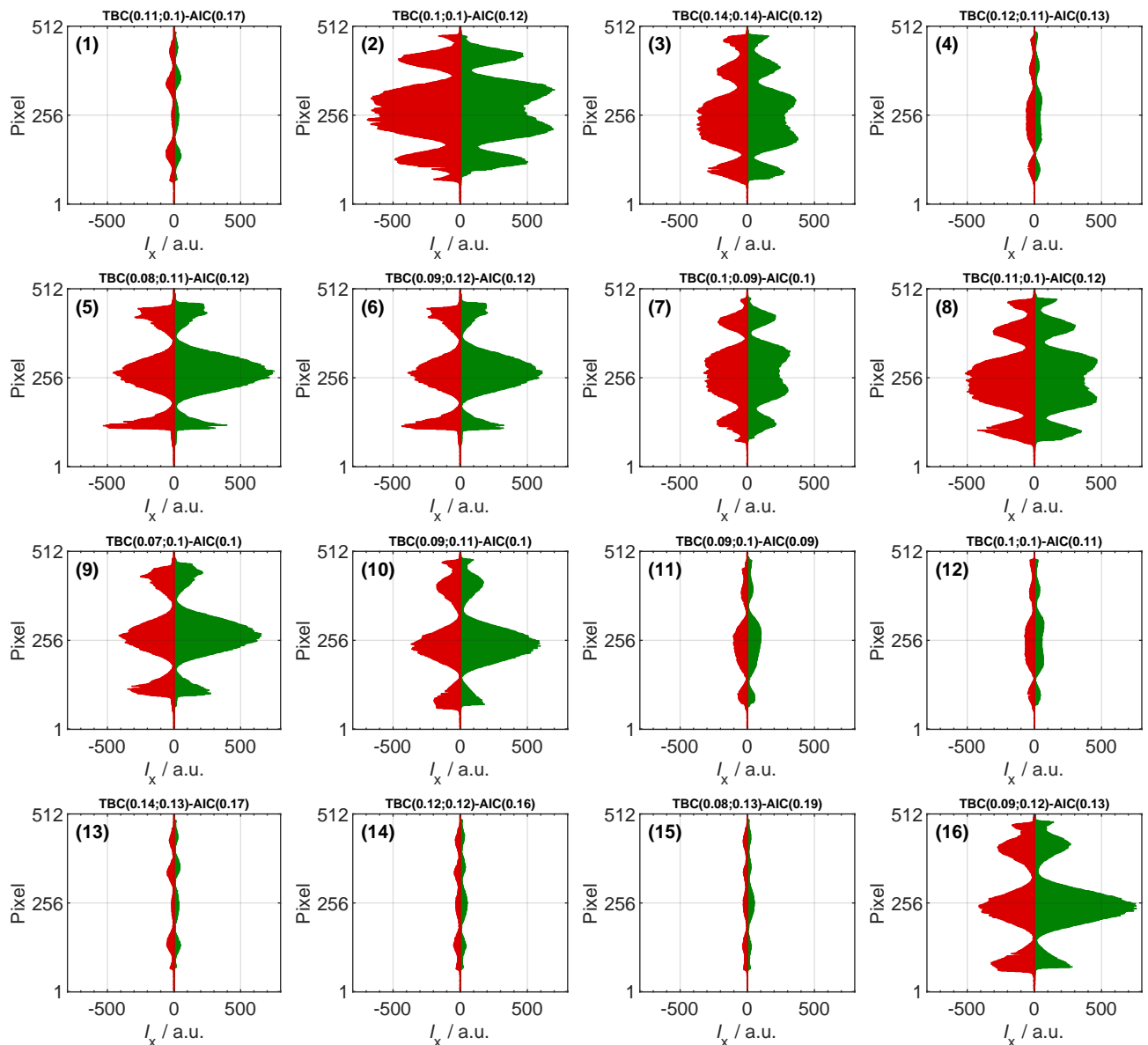


Figure S15. Example scattering patterns of spherical PEG particles. Plots depict the relative light intensity as a function of array pixel number, for array 1 (green) and array 2 (red). The values on top of each panel depict the TBC, where the first number corresponds to array 1 and the second number to array 2, respectively, and the AIC.

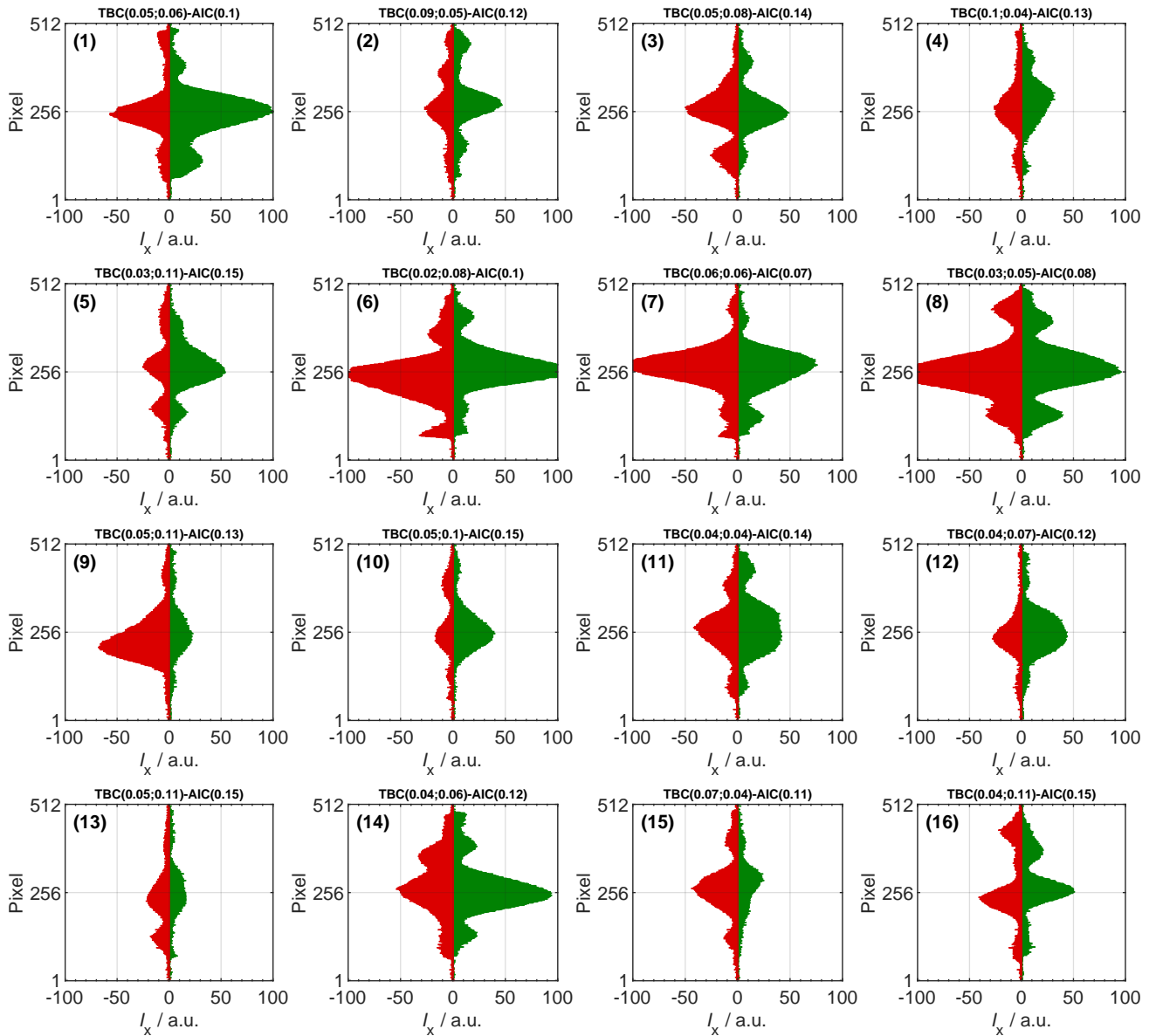


Figure S16. Example scattering patterns of near-spherical NaCl particles, showing relatively low values for the symmetry parameters. Plots depict the relative light intensity as a function of array pixel number, for array 1 (green) and array 2 (red). The values on top of each panel depict the TBC, where the first number corresponds to array 1 and the second number to array 2, respectively, and the AIC.

S7 Random forest model

Figure S17 shows the OOB error of the random forest model, i.e. the fraction of mis-classified particles from the OOB observations, as a function of the number of decision trees considered, for the training data set and using 4 predictors (TBC_1 , TBC_2 , ΔTBC , AIC). The OOB error is high for low tree numbers, but decreases rapidly and levels off around 100 trees, indicating an increased robustness of the ensemble prediction, as more members (trees) are considered. This is consistent with the OOB error converging towards the error of generalization with increasing ensemble members. Given the asymptotic feature of the curve we choose 200 trees for our random forest model due to the sufficiently low OOB error variance reached for classification.

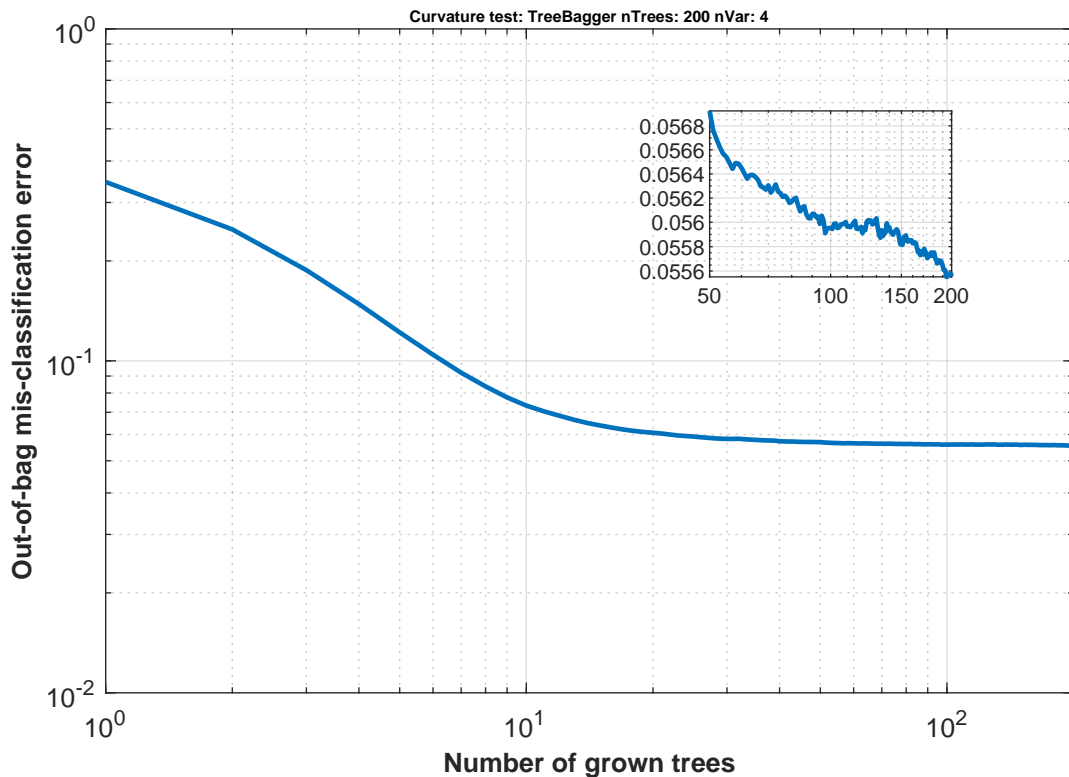


Figure S17. Out-of-bag (misclassification) error of random forest model as a function of the number of trees within the ensemble for the training data set and using 4 predictors as input, using MATLAB's *TreeBagger* algorithm. Inset: enlargement for the range between 50 and 200 trees.

S8 Sizing

The particle sizes determined with PPD-HS, termed instrument response (AD), can differ from the theoretically expected particles sizes, resulting from PPD-HS specific properties, such as variation of the trigger/sizing laser power. Such variation can result in offsets between the determined and expected particle size. In Fig. S18 we show AD as a function of scattering cross section for PEG particles.

5 The scattering cross section is a function of instrument optical geometry (collection angle) and particle properties including size, shape and refractive index. Scattering cross sections were calculated using Mie theory (Bohren and Huffman, 1983) and assuming perfectly spherical particles and refractive indices reported by Ottani et al. (2002), along with mean diameters of the PEG populations.

10 The relation between AD and the scattering cross section is universally valid, such that size calibration can be made particle type-specific if particle refractive indices are known. That is, using the relation between AD and the scattering cross section, we have calculated scattering cross sections for discrete particle diameters, using the particle type specific refractive index, in order to determine size calibration curves (see Fig. 5).

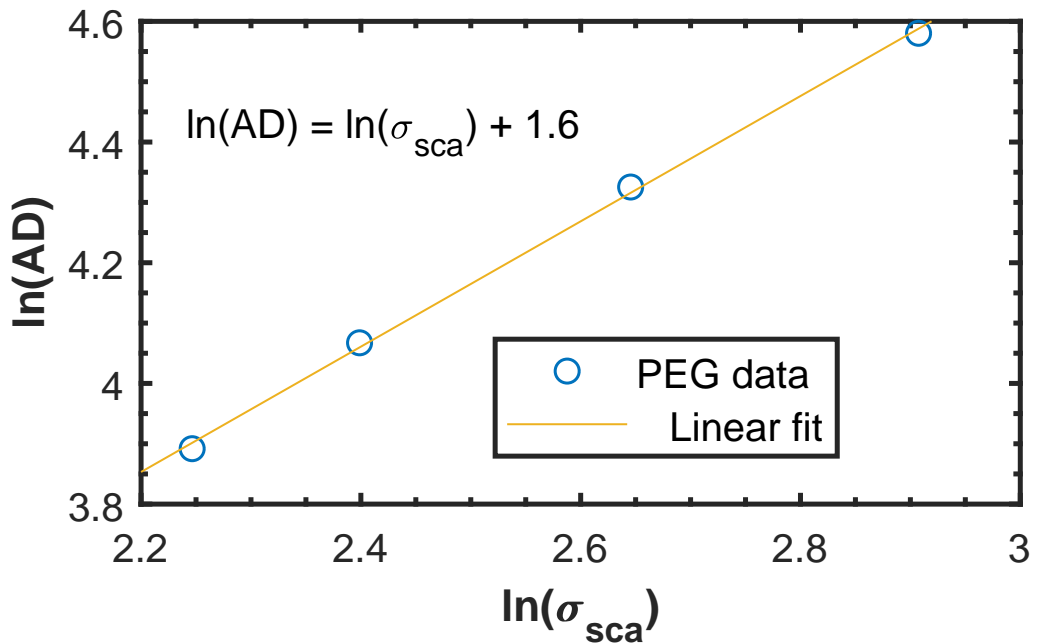


Figure S18. Instrument response (AD) of PPD-HS as a function of particle scattering cross section (σ_{sca}) for PEG particles. The scattering cross section is calculated using Mie theory along with the refractive indices of PEG (see e.g. Ottani et al., 2002) and using the arithmetic mean diameters of the respective PEG populations. The line indicates a linear fit, given by the equation indicates.

S9 HINC-PPD-HS experiments

S9.1 NH₄NO₃

In this section we show exemplified raw scattering patterns for the liquid cloud case of the HINC-PPD-HS experiments using NH₄NO₃, discussed in the main text.

5 In Fig. S19 we show the temporal evolution of particle size, as derived from RT-data, for the pure ice cloud experiment shown in Fig. 7. Size distribution are shown as cumulative density distributions and correspond to particles detected within 1 min intervals, where all particles detected during an interval were binned into 0.25 μm size bins, between 0 and 8 μm .

10 Here, we focus on times between 11:49 and 11:52 am, covering the time period when the majority of particles are correctly classified as aspherical, in order to support our argument in the main text, about asphericity being related to particle size (see main text Fig. 7). Considering the orange and yellow curves, we find minimum particle sizes of approximately 3.2 and 3.4 μm , respectively, for at least 50 % of the particles being larger than that size, assuming these particles to make up the aspherical fraction.

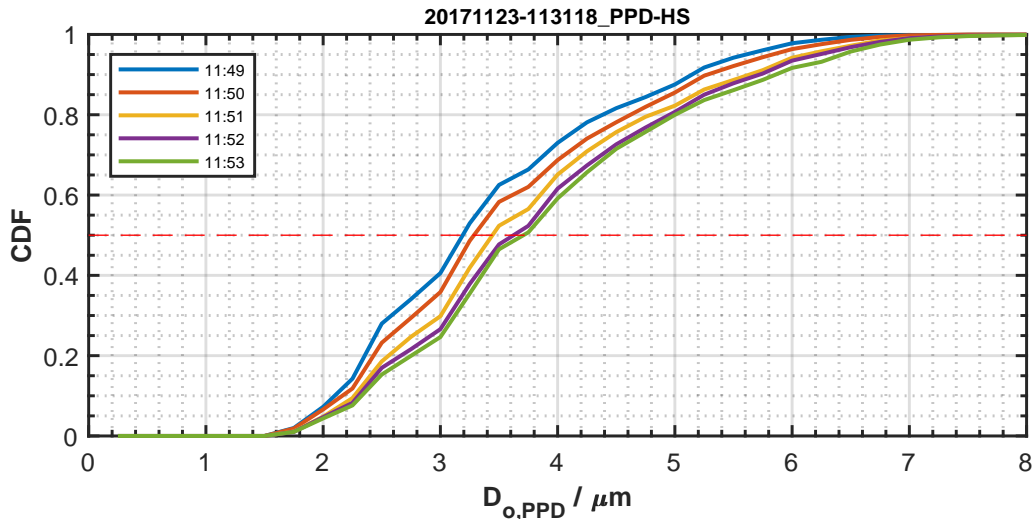


Figure S19. Temporal evolution of particle size distributions derived from the RT-data for the experiment using NH₄NO₃ at $T = 223$ K. Size distributions shown correspond to particles detected within 1 min intervals, with the start time indicated in the legend.

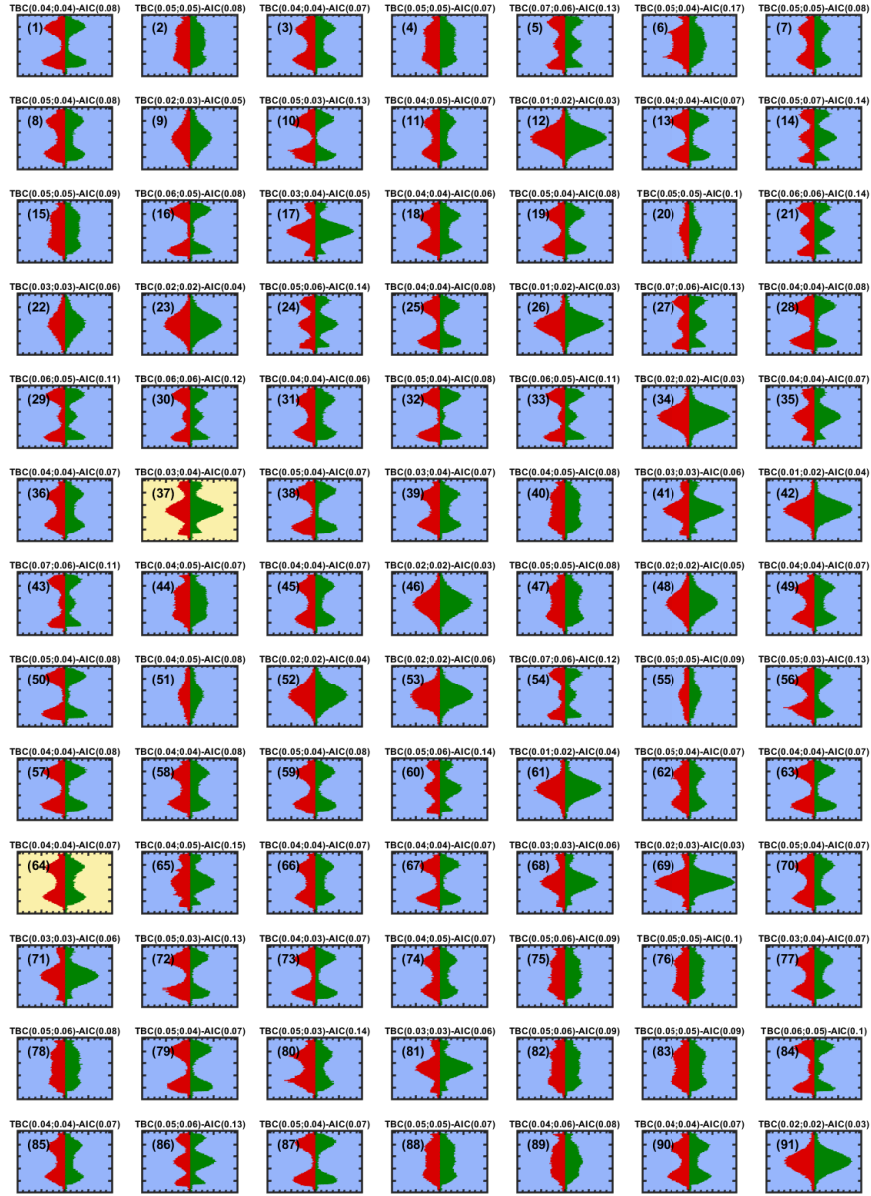


Figure S20. Collection of example particles imaged with PPD-HS during period 1 of the coupled HINC-PPD-HS experiment shown in main text Fig. 10, using NH_4NO_3 at $T = 243$ K. All scattering patterns are shown on the same intensity scale (± 40 a.u.). Background color of the individual scattering patterns indicates particle classification by the random forest model into target classes isSpherical (blue) and isAspherical (yellow).

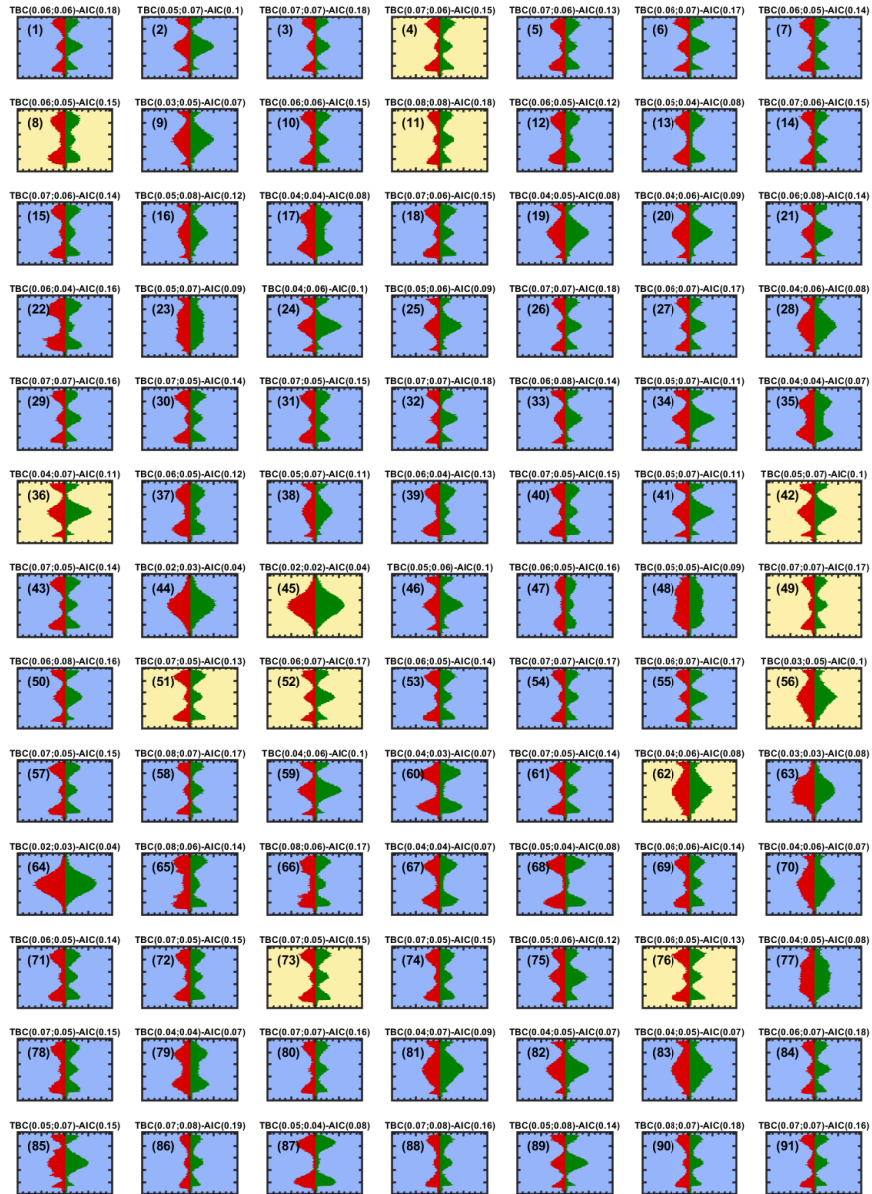


Figure S21. As in Fig. S20, but for period 2.

S9.2 Illite NX

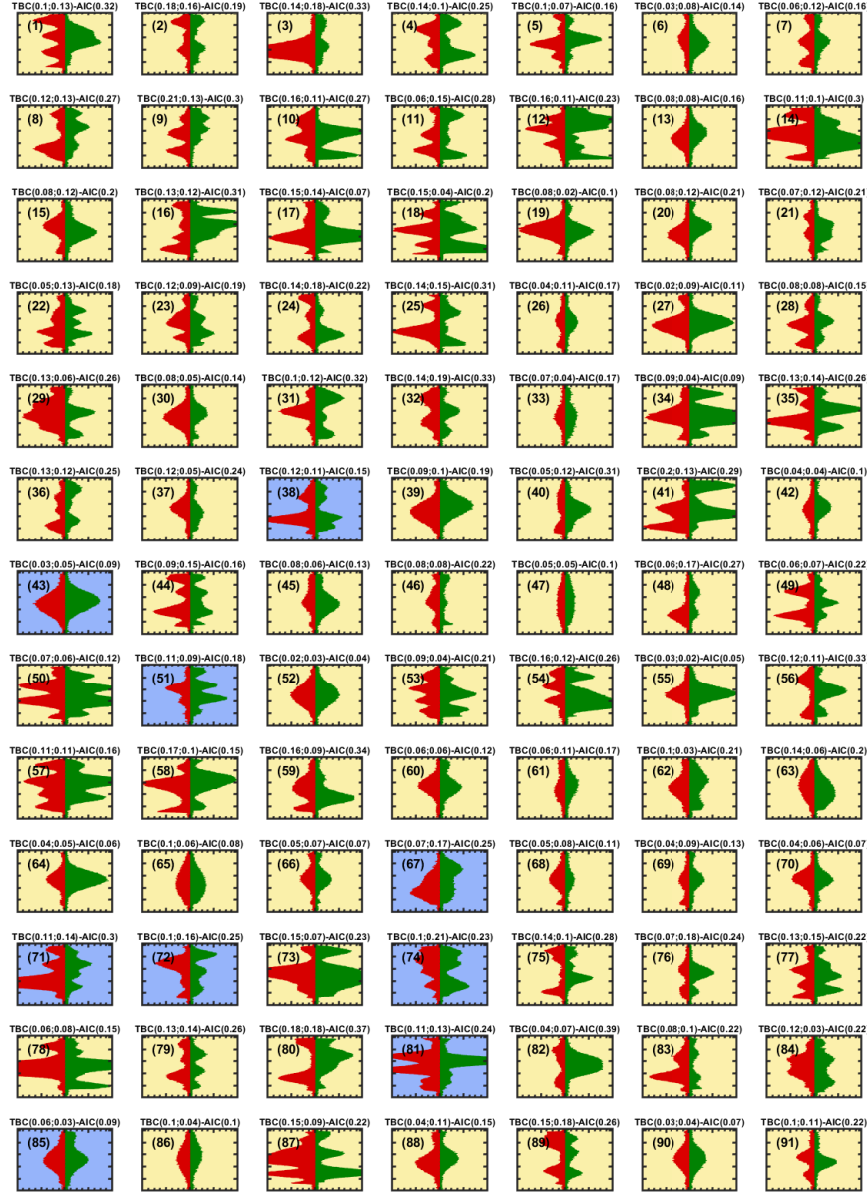


Figure S22. Collection of example particles imaged with PPD-HS during period 1 of the coupled HINC-PPD-HS experiment shown in main text Fig. 7, using illite NX at $T = 238$ K. All scattering patterns are shown on the same intensity scale (± 40 a.u.). Background color of the individual scattering patterns indicates particle classification by the random forest model into target classes isSpherical (blue) and isAspherical(yellow).

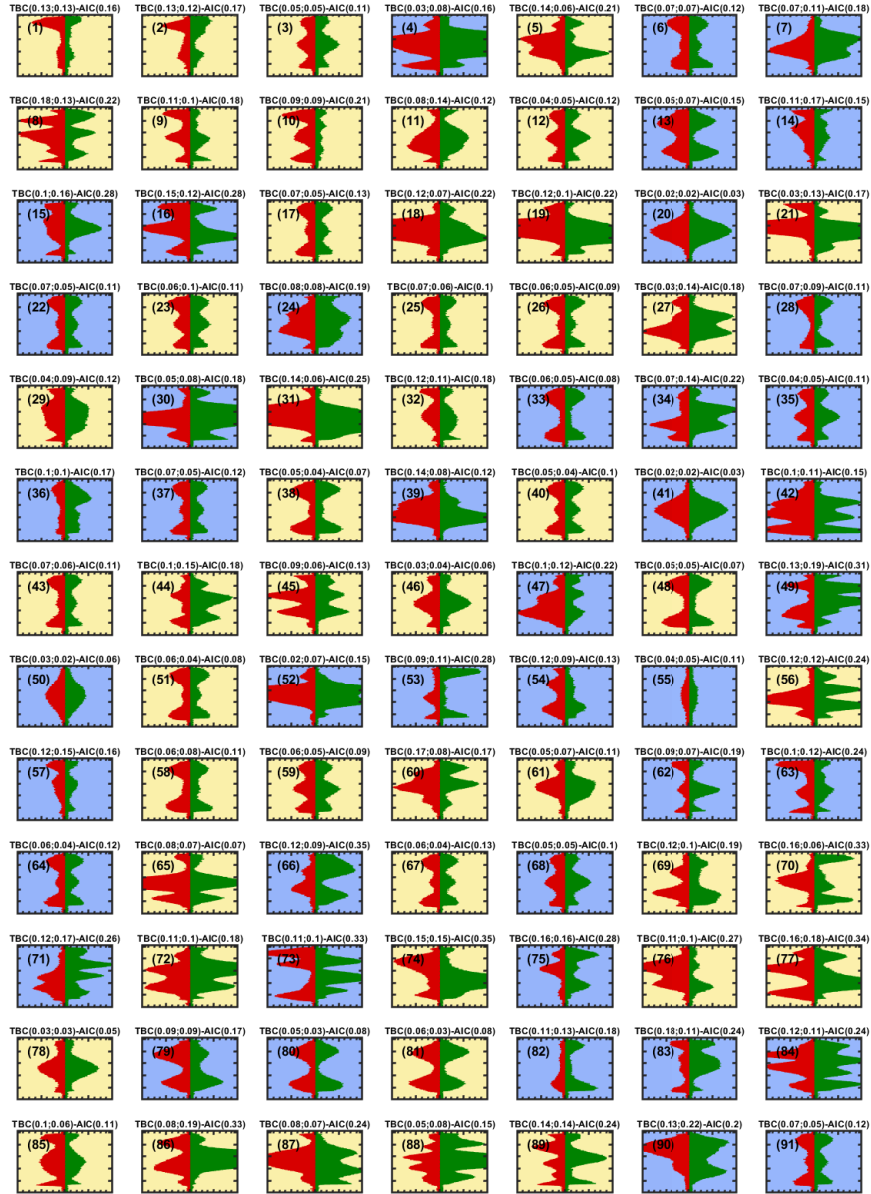


Figure S23. Collection of example particles imaged with PPD-HS during period 2 of the coupled HINC-PPD-HS experiment shown in main text Fig. 7, using illite NX at $T = 238$ K. All scattering patterns are shown on the same intensity scale (± 40 a.u.). Background color of the individual scattering patterns indicates particle classification by the random forest model into target classes isSpherical (blue) and isAspherical (yellow).

References

- Bohren, C. F. and Huffman, D. H.: Absorption and scattering of light by small particles, Wiley Interscience, New York, 1983.
- Johnson, A., Lasher-Trapp, S., Bansemer, A., Ulanowski, Z., and Heymsfield, A. J.: Difficulties in Early Ice Detection with the Small Ice Detector-2 HIAPER (SID-2H) in Maritime Cumuli, *Journal of Atmospheric and Oceanic Technology*, 31, 1263–1275, 2014.
- 5 Ottani, S., Vitalini, D., Comelli, F., and Castellari, C.: Densities, Viscosities, and Refractive Indices of Poly(ethylene glycol) 200 and 400 + Cyclic Ethers at 303.15 K, *Journal of Chemical Engineering Data*, 47, 1197–1204, 2002.